



Article

Maize Crop Detection through Geo-Object-Oriented Analysis Using Orbital Multi-Sensors on the Google Earth Engine Platform

Ismael Cavalcante Maciel Junior ¹, Rivanildo Dallacort ², Cácio Luiz Boechat ³, Paulo Eduardo Teodoro ^{4,*}, Larissa Pereira Ribeiro Teodoro ⁴, Fernando Saragosa Rossi ⁴, José Francisco de Oliveira-Júnior ⁵, João Lucas Della-Silva ⁶, Fabio Henrique Rojo Baio ⁴, Mendelson Lima ⁷, and Carlos Antonio da Silva Junior ^{6,*}

- ¹ Post-Graduate Program in Biodiversity and Amazonian Agroecosystems (PPGBioAgro), State University of Mato Grosso (UNEMAT), Alta Floresta 78580-000, MT, Brazil; cavalcante.ismael@unemat.br
 - ² Department of Agronomy, State University of Mato Grosso (UNEMAT), Tangará da Serra 78301-532, MT, Brazil; rivanildo@unemat.br
 - ³ Department of Agronomy, Federal University of Piauí (UFPI), Bom Jesus 64900-000, PI, Brazil; cacioboechat@ufpi.edu.br
 - ⁴ Department of Agronomy, Federal University of Mato Grosso do Sul (UFMS), Chapadão do Sul 79560-000, MS, Brazil; larissa_ribeiro@ufms.br (L.P.R.T.); fernando.rossi@ufms.br (F.S.R.); fabio.baio@ufms.br (F.H.R.B.)
 - ⁵ Department of Atmospheric Sciences, Federal University of Alagoas (UFAL), Maceió 57480-000, AL, Brazil; jose.junior@icat.ufal.br
 - ⁶ Department of Geography, State University of Mato Grosso (UNEMAT), Sinop 78555-000, MT, Brazil; joao.lucas1@unemat.br
 - ⁷ Department of Biology, State University of Mato Grosso (UNEMAT), Alta Floresta 78580-000, MT, Brazil; mendelson@unemat.br
- * Correspondence: paulo.teodoro@ufms.br (P.E.T.); carlosjr@unemat.br (C.A.d.S.J.)



Citation: Maciel Junior, I.C.; Dallacort, R.; Boechat, C.L.; Teodoro, P.E.; Teodoro, L.P.R.; Rossi, F.S.; Oliveira-Júnior, J.F.d.; Della-Silva, J.L.; Baio, F.H.R.; Lima, M.; et al. Maize Crop Detection through Geo-Object-Oriented Analysis Using Orbital Multi-Sensors on the Google Earth Engine Platform. *AgriEngineering* **2024**, *6*, 491–508. <https://doi.org/10.3390/agriengineering6010030>

Academic Editor: Leonardo Conti

Received: 21 December 2023

Revised: 14 February 2024

Accepted: 19 February 2024

Published: 22 February 2024



Copyright: © 2024 by the authors. Licensee MDPI, Basel, Switzerland. This article is an open access article distributed under the terms and conditions of the Creative Commons Attribution (CC BY) license (<https://creativecommons.org/licenses/by/4.0/>).

Abstract: Mato Grosso state is the biggest maize producer in Brazil, with the predominance of cultivation concentrated in the second harvest. Due to the need to obtain more accurate and efficient data, agricultural intelligence is adapting and embracing new technologies such as the use of satellites for remote sensing and geographic information systems. In this respect, this study aimed to map the second harvest maize cultivation areas at Canarana-MT in the crop year 2019/2020 by using geographic object-based image analysis (GEOBIA) with different spatial, spectral, and temporal resolutions. MSI/Sentinel-2, OLI/Landsat-8, MODIS-Terra and MODIS-Aqua, and PlanetScope imagery were used in this assessment. The maize crops mapping was based on cartographic basis from IBGE (Brazilian Institute of Geography and Statistics) and the Google Earth Engine (GEE), and the following steps of image filtering (gray-level co-occurrence matrix—GLCM), vegetation indices calculation, segmentation by simple non-iterative clustering (SNIC), principal component (PC) analysis, and classification by random forest (RF) algorithm, followed finally by confusion matrix analysis, kappa, overall accuracy (OA), and validation statistics. From these methods, satisfactory results were found; with OA from 86.41% to 88.65% and kappa from 81.26% and 84.61% among the imagery systems considered, the GEOBIA technique combined with the SNIC and GLCM spectral and texture feature discriminations and the RF classifier presented a mapping of the corn crop of the study area that demonstrates an improved and aided the performance of automated multispectral image classification processes.

Keywords: textures GLCM; Landsat-8; MODIS; PlanetScope; random forest; Sentinel 2; SNIC segmentation

1. Introduction

Mato Grosso state is the biggest maize producer in Brazil, according to Companhia Nacional de Abastecimento (Conab) in its 12^o Brazilian grains crop survey (2021/22),

presenting an area of near 6.55 million hectares (ha) and 41.62 million tons (t) of grains [1]. It is also worth noting that despite the large domestic consumption, most of the production is destined for exports, which have broken records in recent years [2]. At the state level, the predominance of cultivation occurs on the second harvest, which corresponds to approximately 99% of the maize crop total area [3]. In view of the large production, the crop area's estimate plays an important role on national demand supply as well as ensuring that transportation and storage capacity are not compromised [4].

Brazilian official crops estimates are based on subjective surveys by Conab and Instituto Brasileiro Geografia e Estatística (IBGE). Most of the agricultural crops data are based on surveys conducted by technical agents, which rely on cultivated areas, production, and economic data from agricultural producers, agricultural inputs sellers, and other related interviews, which are poorly reliable data for such a survey [5].

Field data surveys occur at low frequency and are being gradually reduced by the scarcity of financial and human resources. Moreover, the large territorial extension of the state of Mato Grosso makes the surveys costly and time-consuming. In this way, the use of remote sensing techniques and geographic information systems (GIS) can be applied to avoid the inconveniences related to the search for agricultural production data [6]. In comparison to other productive sectors, agricultural activities face uncertainties and thus demand frequent and large-scale monitoring [7,8].

Remote sensing and geoprocessing are the most use techniques for land use data generation over time, as they allow the evaluation of changes in the landscape [9]. Remote sensing imagery provides important historical series for crop dynamics identification, and spatial resolution allows precision agriculture-level interventions [10]. Geographic object-based image analysis (GEOBIA) has emerged as a powerful methodology for image analysis and classification, proving effective in accurately identifying and classifying land cover types, mapping and monitoring deforestation, monitoring vegetation health and growth, predicting crop yields, and classifying remote sensing imagery [11]. By utilizing spectral, spatial, textural and topological features, GEOBIA enables comprehensive image analysis, providing valuable information about the characteristics of and changes in natural and agricultural landscapes [12].

These methodologies offer strong integration with GIS and use advanced machine learning techniques for image classification. By combining the power of random forest (RF) with the insights derived from GEOBIA, which uses a set of decision trees where each tree is trained on a subset of data and features, providing robust and accurate predictions, researchers and practitioners have achieved significant advances in the analysis of remotely sensed imagery, enabling comprehensive understanding and informed decision making [13,14]. The emergence of several cloud computing platforms, which store images captured by a range of satellite sensors as well as geospatial analysis and geoprocessing tools, has expanded access to free images to supports a wide range of remote sensing research. The Google Earth Engine stands out in this scenario [15]. The platform has imagery data from the Sentinel, Landsat, and Terra/Aqua satellites and provides conditions for the development of geospatial algorithms involving large data sets [16].

In view of the economic importance of maize for Canarana and the Mato Grosso state, information regarding the extension of cultivated areas, which is widely disclosed by the official estimates of area and agricultural production made by IBGE and Conab, supports political and economic planning. However, there are currently differences between these agencies' publications that were evidenced in the 2019/20 harvest. In that crop year, Conab estimated an area of 5414.4 ha [3], while IBGE estimated 5337.3 thousand ha for second-harvest maize cultivation in Mato Grosso [17].

This area difference is one of the factors that contributes to the difference in maize production of about 930,000 tons in the state, which is a significant amount for agribusiness, and this has raised uncertainty in the sector about the numbers released by official agencies. Therefore, this study presents a geoprocessing- and remote-sensing-based approach to mapping maize crops at Canarana in the state of Mato Grosso.

2. Materials and Methods

The mapping of agricultural land with remote sensing tools endorsed by geoprocessing and based on well-established, cost-effective, time-efficient, and accurate machine learning was carried out as determined by the definition of approaches of each of the following steps. Here, the maize crops mapping at Canarana in the state of Mato Grosso considered the steps in the following workflow (Figure 1).

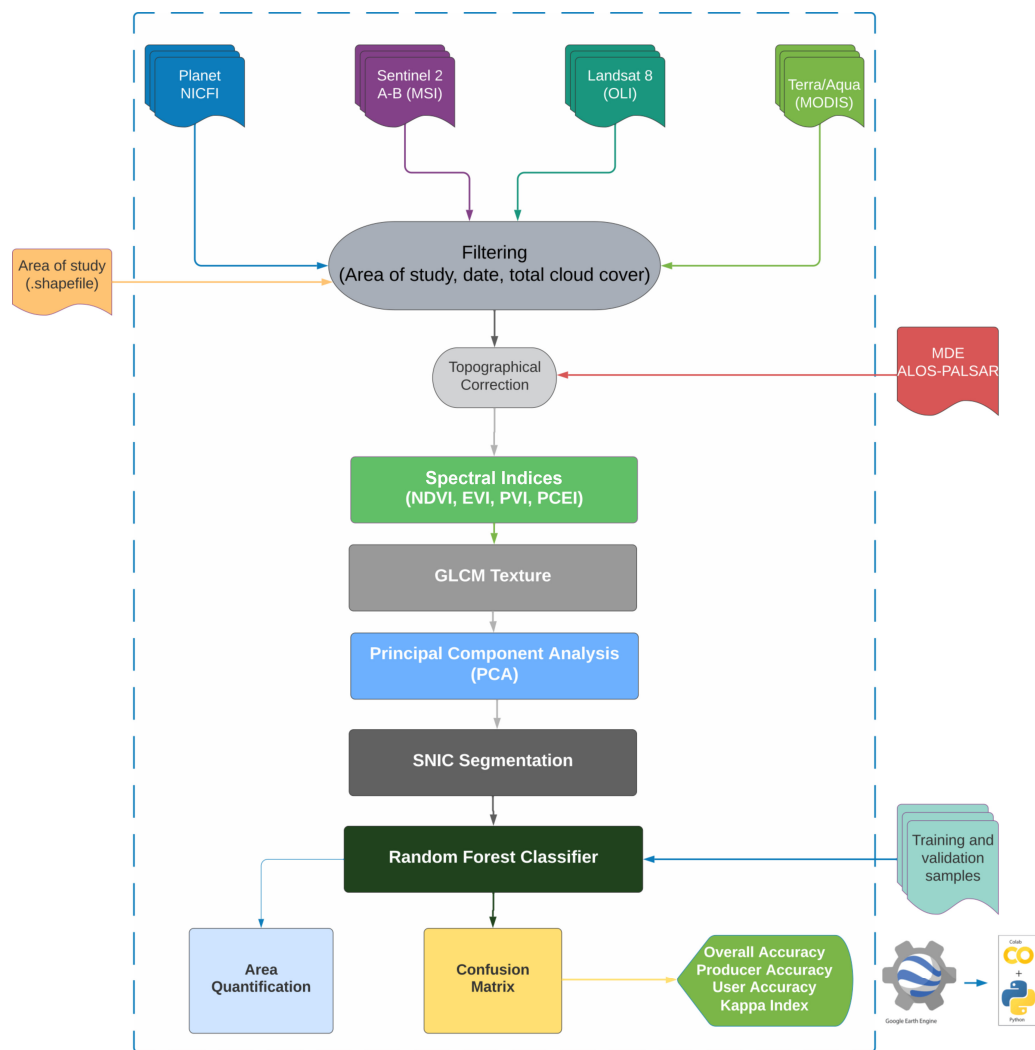


Figure 1. Flowchart of the object-oriented classification methodology.

2.1. Study Area

The study area comprises the municipality of Canarana, in northeastern Mato Grosso, over the geographic coordinates 12°36'17" to 13°47'12" S and 51°22'32" to 53°06'12" W (Figure 2). Canarana has an area of 10,855.181 km² and estimated population of 21,842 inhabitants. The average altitude of the locality is 390 m, and it is characterized by a humid tropical climate (Köppen–Geiger climate classification: Aw), with mean temperature of 25 °C. It exhibits two well-defined seasons, namely dry (from May to September) and rainy (from October to April) [18,19], with an average annual rainfall for the 2019/2020 crop year ranging around 1650.54 mm to 1866.10 mm [20]. The predominant soil class is dystrophic red-yellow latosol [21].

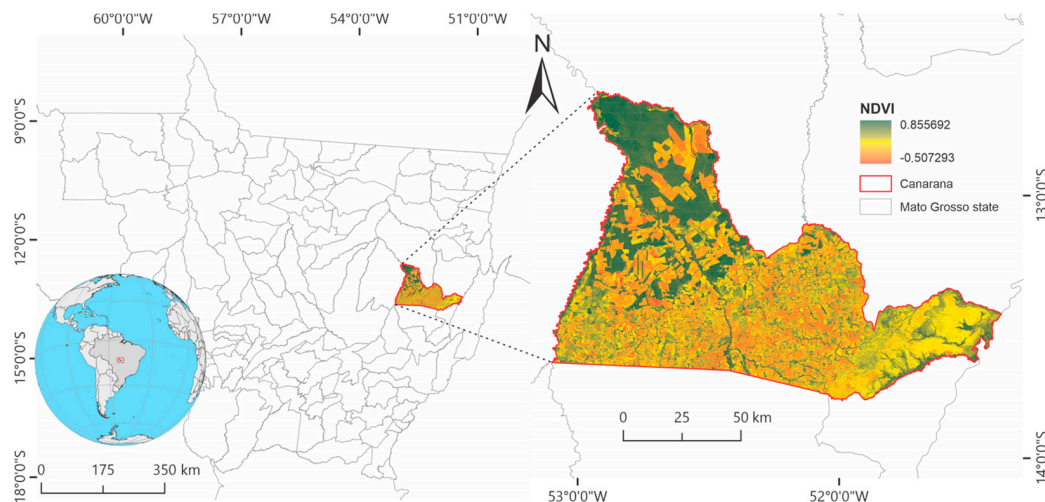


Figure 2. Location of study area in Canarana municipality, Mato Grosso state, presented by using the normalized difference vegetation index (NDVI).

Canarana was involved in the Superintendence for the Development of Amazon (SUDAM), originated in 1972 from a colonizing cooperative company (Cooperativa Colonizadora 31 de Março Ltd.a—COOPERCOL) appliance. The purpose of the project was to attract to the regional rural entrepreneurs (large, medium, and small) as well as the multinational and family producers. Currently, the main economic activities of the municipality are cattle ranching, agriculture (rice, maize, sesame, and soy), and agroindustry. In view of agricultural aptness and phytogeography, the Amazon–Cerrado biomes transition can be seen in the Canarana area, where 34.51% is attributable to the Amazon biome and 65.49% to Cerrado [18,19,22,23].

2.2. Pre-Processing

At first, the IBGE cartographic basis for Canarana was followed, based upon the methodological approach, and then Google Earth Engine (GEE) uploading was carried out. Due to processing limitations in the GEE platform resources, the acquisition, segmentation, and machine learning steps for processing geospatial data were performed in the Google Collaboratory platform (Colab) and can be accessed at <https://colab.research.google.com/> (accessed on 12 November 2022). The Google Colab platform is based on the Python language in the Jupyter Notebook, allowing free access at runtime to scripts. The PlanetScope NICFI imagery was added to GEE in addition to other multispectral imagery present in Google Earth Engine, namely MODIS Terra/Aqua, OLI/Landsat-8 (Operational Land Imager), and MSI/Sentinel-2 (MultiSpectral Instrument). Multiple imagery-based stages in this methodological approach were utilized for maize crops detection.

Regarding the maize phenological cycle, images from 1 April 2022 to 31 May 2022 were considered since this period represents the stage of greatest vegetative vigor typical of the second-crop maize culture, and these images utilized cloud filtering of up to 35%. In order to obtain a single image to represent the collected period, the median was used.

To reduce the effects of terrain irregularity, before calculating the subsequent spectral indices and image classification, it was necessary to perform topographic correction on GEE [24,25]. This correction was based on a semi-empirical method that takes into account the topography of the area and the solar angle (zenith and azimuth), called the correction method Solar Canopy Sensor+C (SCSc) [25–27]. The SCSc+C model is based on the canopy, allowing changes in the direction of illumination to be considered during the processing of light correction from inclined to horizontal surfaces.

The digital elevation model (DEM) information was taken from the Shuttle Radar Topography Mission (SRTM); the SRTM V3 (SRTM Plus) product was provided by NASA JPL, with a resolution of 1 arc second (approximately 30 m) [28,29]. The SRTM metadata

were used to obtain information such as the satellite angle at solar zenith for topographic correction effectiveness.

Mapping maize crops was dependent on the vegetation indices (VI). Therefore, the NDVI (Equation (1)) was considered since this VI creates an image displaying the green tone (relative biomass), illustrating the contrast of the chlorophyll pigment absorption characteristics in the red band and the high reflectivity of plant materials in the near-infrared band (NIR) [30].

The enhanced vegetation index (EVI) (Equation (2)) was also considered. Despite being similar to Normalized Difference Vegetation Index (NDVI), the EVI is improved in regards to the soil and atmospheric effects for vegetation mapping, and it also does not saturate dense green vegetation areas [30]. Further, the perpendicular vegetation index (PVI) (Equation (3)) allows to nullify the background reflectance of soil a at the crop emergence stage; an important part of this reflectance registered by the sensor refers to exposed soil. Finally, the perpendicular crop enhancement index (PCEI) (Equation (4)) was used to determine the minimum and maximum crop development period [30].

$$NDVI = \frac{\rho_{NIR} - \rho_{RED}}{\rho_{NIR} + \rho_{RED}} \quad (1)$$

$$EVI = g \times \frac{\rho_{NIR} - \rho_{RED}}{\rho_{NIR} + (c_1 \times \rho_{RED}) - (c_2 \times \rho_{BLUE}) + 1} \quad (2)$$

$$PVI = \frac{\rho_{NIR} - (a \times \rho_{RED}) - b}{\sqrt{1 + a^2}} \quad (3)$$

$$PCEI = g \times \frac{(MaxPVI + S) - (MinPVI + S)}{(MaxPVI + S) + (MinPVI + S)} \quad (4)$$

where:

ρ_{NIR} —Reflectance in the near-infrared spectral range;

ρ_{RED} —Reflectance in the red spectral range;

ρ_{BLUE} —Reflectance in the blue spectral range;

g —Gain factor (10^2);

c_1 —Atmospheric effects correction coefficient for red (6.0);

c_2 —Atmospheric effects correction coefficient for blue (7.5);

a —Soil line slope (1.17);

b —Soil line intercept (3.37);

MaxPVI—Maximum PVI value observed during the period of maximum maize crop development;

MinPVI—Minimum PVI value observed in the pre-planting and/or emergence period;

S —Enhancement coefficient. (the value of 10^2 is assigned for the enhancement of the amount of energy deposited in the active layer of the cell due to the reduction of the reflection intensity.)

2.3. Segmentation and Classification

The segmentation and classification process were initially based on textural feature extraction via gray level co-occurrence (GLCM). The GLCM statistical approach relies on the texture features from the distribution of observed intensity combinations at specified positions relative to each other in the same image (Equations (5)–(9)) [31,32]. This algorithm requires an eight-bit gray-level image generated by linearly combining near-infrared, red, and green bands, which leads to eighteen different textural indices [25,33]. From this, three texture models were selected: inverse difference moment (IDM), sum of entropy (SENT), and dissimilarity (DISS) [34].

$$mean = \frac{1}{\#P_{Obj}} \sum_{(x,y) \in P_{Obj}} C_k(x,y) \quad (5)$$

$$Standard\ deviation = \sqrt{\frac{1}{\#P_{Obj}} \sum_{(x,y) \in P_{Obj}} \left(c_k(x,y) - \frac{1}{\#P_{Obj}} \sum_{(x,y) \in P_{Obj}} c_k(x,y) \right)^2} \quad (6)$$

$$GLCM\ homogeneity = \sum_{i,j=0}^{N-1} \frac{P_{ij}}{1 + (i - j)^2} \quad (7)$$

$$GLCM\ dissimilarity = \sum_{i,j=0}^{N-1} P_{ij} |i - j| \quad (8)$$

$$GLCM\ entropy = \sum_{i,j=0}^{N-1} P_{ij} (-\ln P_{ij}) \quad (9)$$

where:

P_{Obj} — $\{(x, y): (x, y) \in P_{Obj}\}$ Set of pixels of an image object;

$\#P_{Obj}$ —Total number of pixels contained in the P_{Obj} ;

$c_k(x, y)$ —Pixel value of the image layer (x, y) , where (x, y) are pixel coordinates;

i —Row number of the co-occurrence matrix;

j —Column number of the co-occurrence matrix;

$P_{i,j}$ —The normalized value in the cell i, j : $P_{i,j} = \left(V_{i,j} / \sum_{i,j=0}^{N-1} V_{i,j} \right)$;

$V_{i,j}$ —The value in cell i, j of the co-occurrence matrix;

N —The number of rows or columns of the co-occurrence matrix.

After the procedure, the principal component (PC) analysis was carried out in view of data dimensionality reduction to maximize the amount of original information in the smallest number of principal components. Here, the data rely on 16 vectors among bands, vegetation indices, and texture features [25,35].

This process significantly reduces the computational burden for feature extraction by transforming a set of correlated variables (original bands) into distinct uncorrelated variables (principal components) that contain a maximum of primary information, significantly speeding up the maximum likelihood classification process [36]. Moreover, these calculations have been widely applied in remote sensing to classify land use and land cover and their changes [35,37].

Next, the images went through the segmentation step, qualified by the application of the simple non-iterative clustering (SNIC) algorithm [38]. In this algorithm, similar pixels are grouped into image objects, possessing spectral and textural information that will be employed in the classification step. SNIC is an improved version of the simple linear iterative clustering (SLIC) segmentation algorithm that benefits from a non-iterative procedure and imposes the connectivity rule from the initial stage [34].

At first, SNIC initializes the centroids of pixels in the regular image grid, and the pixel distance in dimensional color space and spatial coordinates are used to determine the dependence of each pixel on the centroid. Finally, the integrated spatial and color distances result in efficient, compact, and nearly uniform polygons, providing the identification of objects (clusters) according to the input parameters and generating a multi-band raster including clusters and additional layers containing average values of the input features [25,33,39,40]. The main parameters of the SNIC algorithm are image, size, compression, connectivity, neighborhood size, and seeds [39,40].

The classification based on the random forest (RF) classifier was applied due to its great accuracy classification compared to other classifiers and also considering the dataset traits and the applied methods [25,33,39–42] in addition to providing a reduced probability of explanatory variables to the training data and fitting them perfectly, regardless of the

large number of decision trees, where each element uses a random subset of the training data and a limited number of randomly selected predictor variables [43].

2.4. Segmentation and Classification

We collected 2200 random field points of maize crops and other different land-use and land-cover types. For this, 74 points of water, 8 of cotton, 10 of agricultural expansion area, 9 of recovering area, 6 of urban area, 239 of Cerrado, 7 of crotalaria, 4 of beans, 347 of forest, 247 of sesame, 84 of millet, 725 of second-crop corn, 159 of pasture, 149 of degraded pasture, 14 of fallow soil, 4 of exposed soil, and 104 of sorghum for the RF training and validation were determined (Figure 3). The Locus Map application was used to collect these points with an average precision of 5 m. For each class of samples, we used 70% of the points in the training phase and 30% in the validation phase; these were selected randomly [25,33,40].

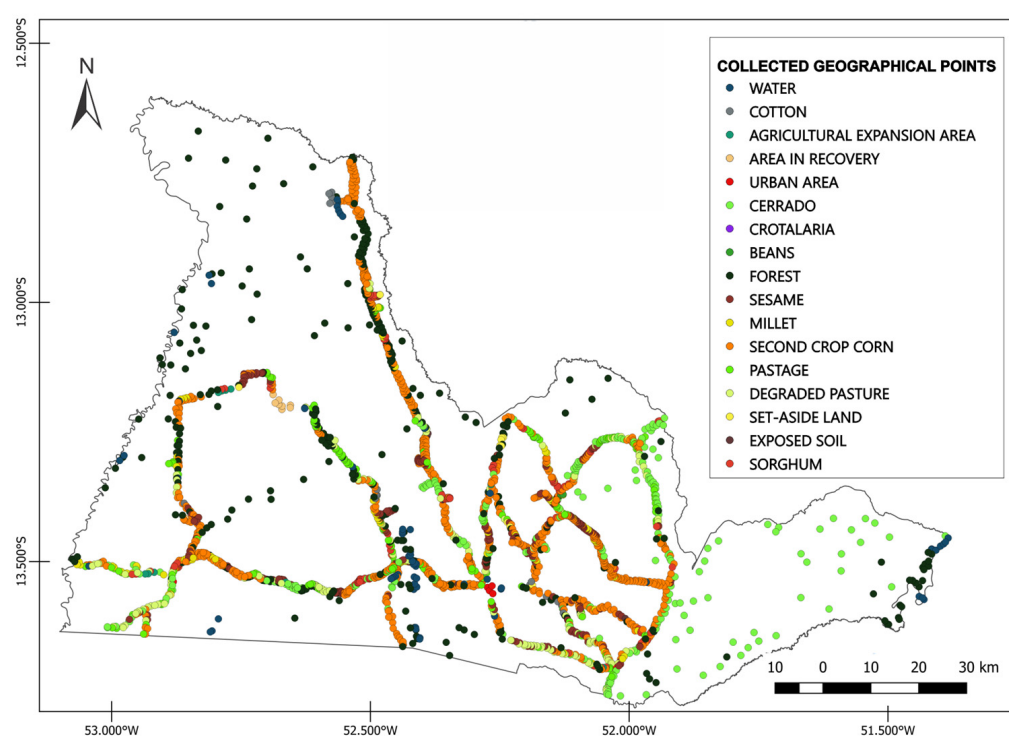


Figure 3. Land-use and land-cover sample's location at Canarana-MT.

After processing and classifying the images and obtaining the thematic maps of the corn areas, we proceeded to the analysis of the numerical confusion matrix, which is responsible for determining the method's accuracy by comparing the percentage of objects classified by class with the real class verified in the field, indicating a posteriori the correct evaluation and errors among the strata studied. The confusion matrix provides the classification's overall accuracy (OA) (Equation (10)); the producer accuracy (PA) (Equation (11)) or omission error that, in turn, indicates the probability that the result classified in the image actually represents that category in reality; and the user accuracy (UA) (Equation (12)) or commission error, which indicates the percentage of correctness of a polygon or a true pixel (reference) to have been correctly classified [25,33,39,40,44,45]. In addition to these analyses, kappa coefficient metrics (Equation (13)) were applied to assess the reliability and accuracy of the classified data [46].

$$OA (%) = \frac{\sum_{i=1}^n P_{ii}}{N} \times 100, \tag{10}$$

$$PA (%) = \frac{P_{ii}}{P_{+i}} \times 100 \tag{11}$$

$$UA (%) = \frac{P_{ii}}{P_{i+}} \times 100, \tag{12}$$

$$kappa (%) = \frac{N \times \sum_{i=1}^n P_{ii} - \sum_{i=1}^n (P_{i+} \times P_{+i})}{N^2 - \sum_{i=1}^n (P_{i+} \times P_{+i})} \times 100 \tag{13}$$

where:

- n—Total number of columns in the confusion matrix, i.e., the total number of categories;
- P_{ii} —Number of correct classifications of the top crop type sample in row i and column i of the confusion matrix;
- P_{i+} —Total number of samples of the crop type in row i ;
- P_{+i} —Total number of samples of the culture type in column i ;
- N —Total amount of samples used for verification.

3. Results and Discussion

Through the digital elevation model, two land-use classes were derived with a 12% slope threshold based on the mechanization factor as one of the attributes to be observed in the agricultural aptitude and considering that some machines, mainly harvesters, that are available on the market are adapted for slopes of up to 12% [47–49]. The area amount of 10,465.36 km² with up to 12% slope was obtained, corresponding to 96.55% of the total area of the municipality.

For improving supervised classification results, PC analysis was carried out, and as input, the reflectance data of 16 bands based on red (R), green (G), blue (B), and near-infrared (NIR) bands of the four sensors as well as the terrain slope and the vegetation indices were utilized. Here, the first three components (PC1, PC2, and PC3) were defined, which can express the dataset variance (Table 1).

Table 1. Principal component variation in each sensor.

PC	OLI/Landsat-8	MODIS	PlanetScope	MSI/Sentinel-2
PC01	97.02%	94.52%	98.22%	95.28%
PC02	2.65%	4.31%	1.52%	4.51%
PC03	0.29%	1.08%	0.18%	0.15%
PC04	0.03%	0.04%	0.04%	0.03%
PC05	0.01%	0.03%	0.03%	0.02%
PC06	0.00%	0.02%	0.01%	0.01%
PC07	0.00%	0.00%	0.00%	0.00%
PC08	0.00%	0.00%	0.00%	0.00%
PC09	0.00%	0.00%	0.00%	0.00%
PC10	0.00%	0.00%	0.00%	0.00%
PC11	0.00%	0.00%	0.00%	0.00%
PC12	0.00%	−0.00%	0.00%	0.00%
PC13	0.00%	−0.00%	0.00%	0.00%
PC14	−0.00%	−0.00%	0.00%	−0.00%
PC15	−0.00%	−0.00%	0.00%	−0.00%
PC16	−0.00%	−0.00%	−0.00%	−0.00%

Our results corroborate other findings [33,35,50] that obtained more than 90% of the information of the original bands in the first three principal components, which can be expressed in false-color composition as shown in Figure 4.

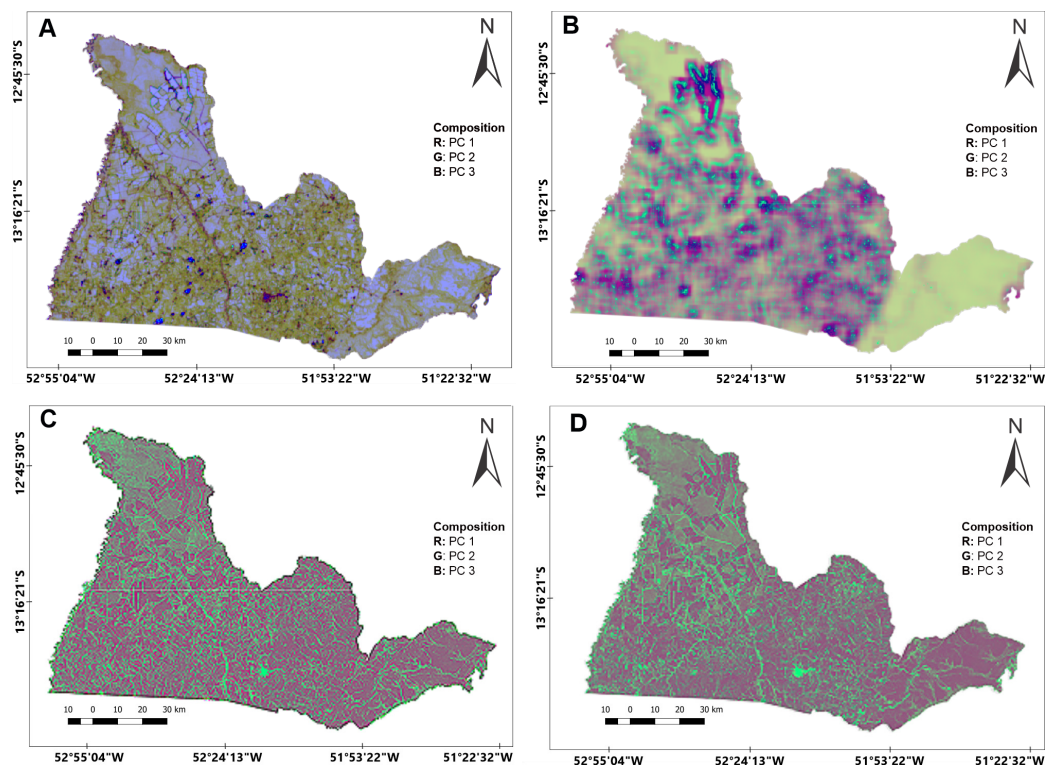


Figure 4. PC analysis mosaicking for (A) OLI/Landsat-8, (B) MODIS Terra, (C) Planet NICFI, and (D) MSI/Sentinel-2.

Hereinafter, the segmentation based on first three principal components was carried out. The combination of texture features with vegetation indices, the original bands, and the PC analysis improved the segmentation results [33].

In the segmentation, one of the factors that may have influenced the results was the decrease of the spatial resolution of the MSI/Sentinel-2 and Planet NICFI sensor images to 30 m, making it possible to evaluate the spectral, textural, contextual characteristics, and hierarchical features of all multispectral images. Also, the limitation of the processing capacity of the GEE platform in the free account was a constraint since the platform is of global use, and therefore free access should be limited [33,51–53].

In a previous step of the final classification of the algorithm, the accuracy test with different numbers of decision trees in random forest showed different results for the four sensors used, which were analyzed a range from 10 (ten) to 200 (two hundred) trees as the ideal combination in terms of accuracy and computational costs [33].

In view of highest accuracy of random forest classification, the optimal quantities of decision trees for imagery sensor were 120, 110, 150, and 180 for OLI/Landsat-8, MODIS, Planet NICFI, and MSI/Sentinel-2, respectively (Figure 5). This process concomitantly evaluated the importance of each image band for land-use and land-cover classification.

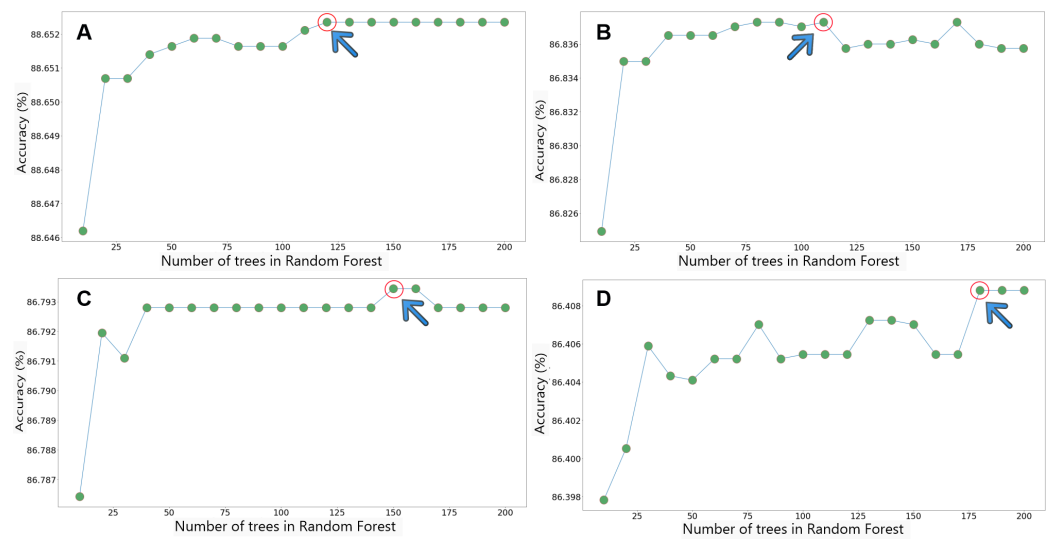


Figure 5. Accuracy test with different quantities of decision trees in the random forest classification process in each imagery system considered: (A) OLI/Landsat-8, (B) MODIS Terra, (C) Planet NICFI, and (D) MSI/Sentinel-2.

From the classified data (Figures 6 and 7), the confusion matrices were generated with OA from 86.41% to 88.65% (Figures 8–11; Table 2). The Landsat imagery had the highest accuracy, with OA ranging from 88.65% to 84.61% and PAs between 65.16% and 91.53%. Yet, the lower accuracy relied on the “other land uses” class, and the higher corresponded to the second-harvest maize class, where UA for this class was 91.98%. [53–55].

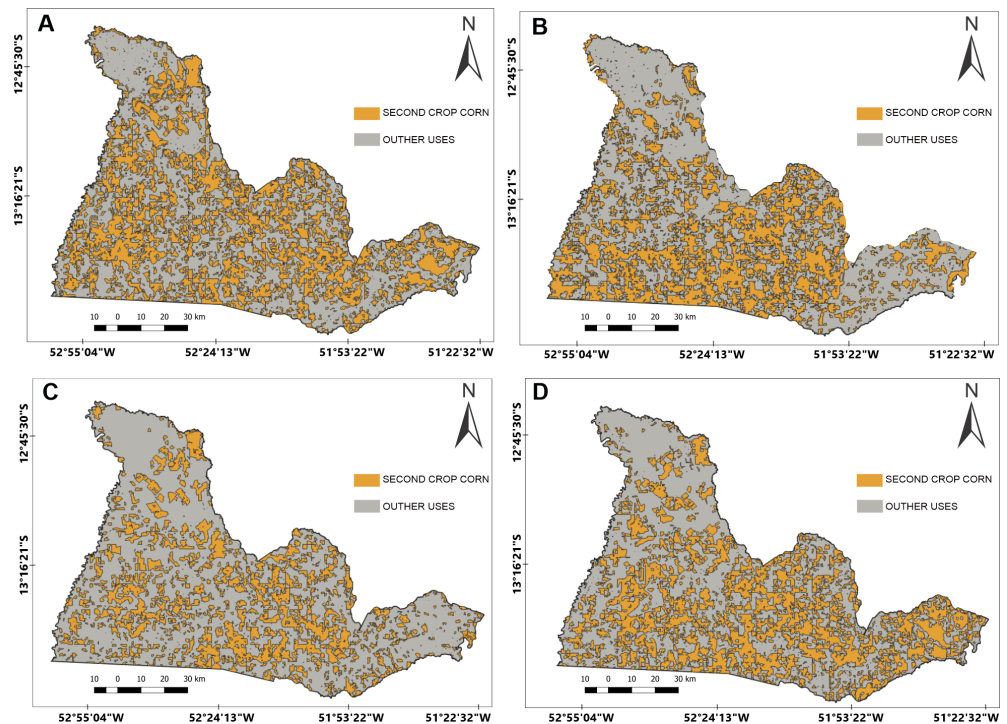


Figure 6. Land-use and land-cover classification based on GEOBIA and random forest for each considered sensor: (A) OLI/Landsat-8, (B) MODIS (C) Planet NICFI, and (D) MSI/Sentinel-2.

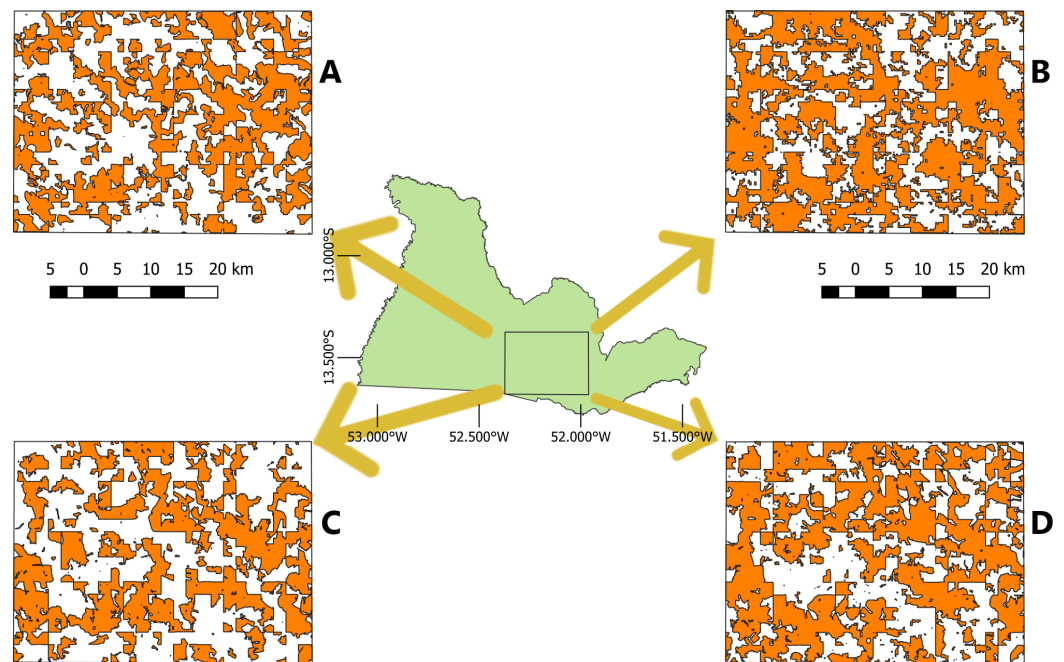


Figure 7. Classified second-crop maize areas clip: (A) OLI/Landsat-8, (B) MODIS, (C) Planet NICFI, and (D) MSI/Sentinel-2.

REFERENCE	WATER	4390 1.04%	172 0.04%	6 0.00%		738 0.17%	5306 82.74% 17.26%	
	NATIVE FOREST	6 0.00%	70176 16.60%	3380 0.80%	3759 0.89%	2 0.00%	3446 0.82%	80769 86.88% 13.12%
	SECOND CROP CORN	790 0.19%	3190 0.75%	144817 34.26%	6882 1.63%	11 0.00%	2511 0.59%	158201 91.54% 8.46%
	OTHER CROPS		2230 0.53%	6233 1.47%	77292 18.29%		3321 0.79%	89076 86.77% 13.23%
	OTHER USES			8 0.00%	1292 0.31%	2462 0.58%	16 0.00%	3778 65.17% 34.83%
	PASTAGE	199 0.05%	1673 0.40%	2997 0.71%	5093 1.20%	8 0.00%	75569 17.88%	85539 88.34% 11.66%
		5385 81.52% 18.48%	77441 90.62% 9.38%	157441 91.98% 8.02%	94318 81.95% 18.05%	2483 99.15% 0.85%	85601 88.28% 11.72%	422669 88.65% 11.35%
	WATER	NATIVE FOREST	SECOND CROP CORN	OUTHER CROPS	OUTHER USES	PASTAGE		
	PREDICTION							

Figure 8. Confusion matrix for OLI/Landsat-8 imagery.

REFERENCE	WATER	4218 1.09%	98 0.03%	18 0.00%	21 0.01%	1206 0.31%	5561 75.85% 24.15%	
	NATIVE FOREST	311 0.08%	60565 15.58%	4376 1.13%	3790 0.97%	7 0.00%	695 0.18%	69744 86.84% 13.16%
	SECOND CROP CORN	1063 0.27%	2893 0.74%	135512 34.86%	8628 2.22%	5 0.00%	3486 0.90%	151587 89.40% 10.60%
	OTHER CROPS	28 0.01%	3848 0.99%	6887 1.77%	75319 19.38%		3450 0.89%	89532 84.13% 15.87%
	OTHER USES			18 0.00%	910 0.23%	1917 0.49%	28 0.01%	2873 66.72% 33.28%
	PASTAGE	65 0.02%	3986 1.03%	2339 0.60%	2545 0.65%	468 0.12%	60042 15.45%	69445 86.46% 13.54%
		5685 74.20% 25.80%	71390 84.84% 15.16%	149150 90.86% 9.14%	91213 82.57% 17.43%	2397 79.97% 20.03%	68907 87.13% 12.87%	388742 86.84% 13.16%
	WATER	NATIVE FOREST	SECOND CROP CORN	OUTHER CROPS	OUTHER USES	PASTAGE		
PREDICTION								

Figure 9. Confusion matrix for MODIS imagery.

REFERENCE	WATER	5049 1.07%	53 0.01%	12 0.00%	21 0.00%	60 0.01%	5195 97.19% 2.81%	
	NATIVE FOREST	458 0.10%	76492 16.25%	5216 1.11%	4457 0.95%	21 0.00%	1238 0.26%	87882 87.04% 12.96%
	SECOND CROP CORN	719 0.15%	2899 0.62%	154116 32.74%	11237 2.39%	31 0.01%	3672 0.78%	172674 89.25% 10.75%
	OTHER CROPS	6 0.00%	483 0.10%	12288 2.61%	95727 20.34%		5062 1.08%	113566 84.29% 15.71%
	OTHER USES		15 0.00%	36 0.01%	1297 0.28%	3338 0.71%	6 0.00%	4692 71.14% 28.86%
	PASTAGE	443 0.09%	3001 0.64%	5395 1.15%	3996 0.85%	36 0.01%	73780 15.68%	86651 85.15% 14.85%
		6675 75.64% 24.36%	82943 92.22% 7.78%	177063 87.04% 12.96%	116735 82.00% 18.00%	3426 97.43% 2.57%	83818 88.02% 11.98%	470660 86.79% 13.21%
	WATER	NATIVE FOREST	SECOND CROP CORN	OUTHER CROPS	OUTHER USES	PASTAGE		
PREDICTION								

Figure 10. Confusion matrix for Planet NICFI imagery.

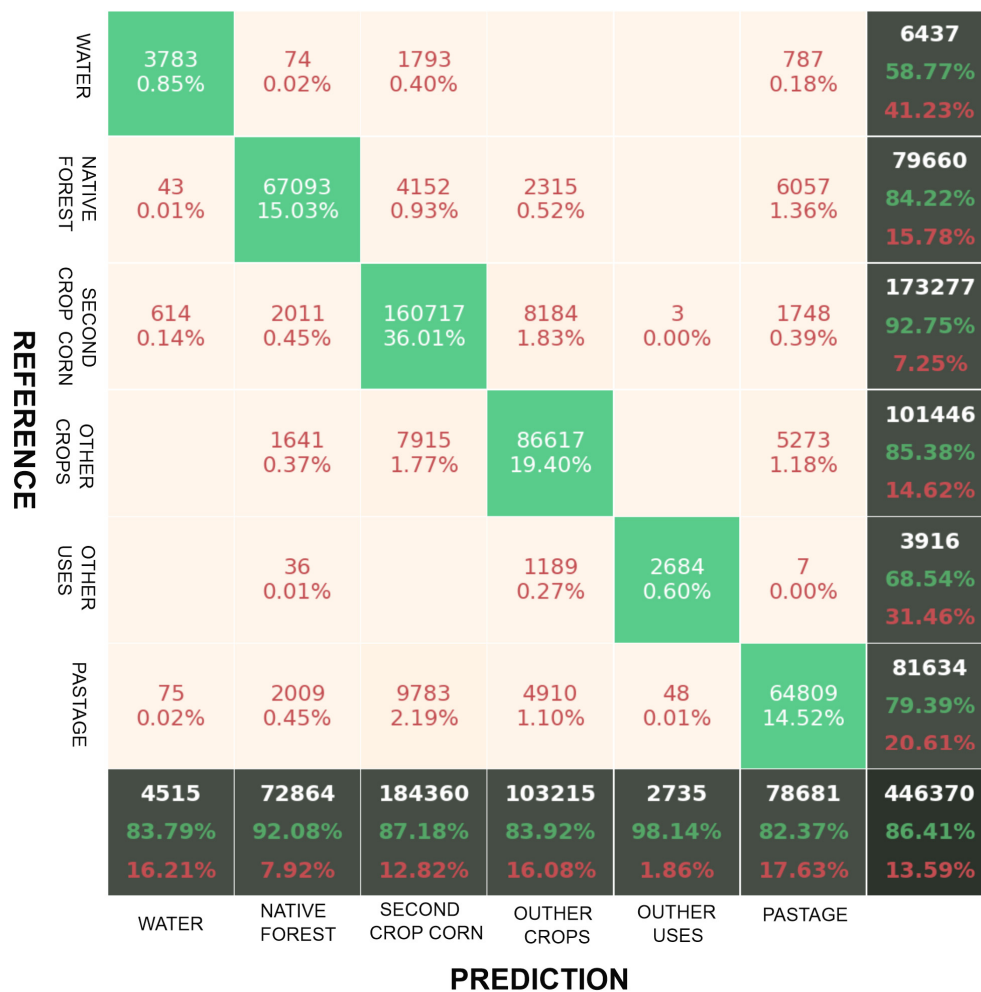


Figure 11. Confusion matrix for MSI/Sentinel-2.

Table 2. Overall accuracy (OA), kappa coefficient, and classified maize crop area (ha) for each sensor image classification.

	Landsat-8	MODIS	Planet	Sentinel-2
Overall accuracy	88.65%	86.83%	86.79%	86.41%
Kappa coefficient	84.61%	82.01%	82.06%	81.26%
Second-harvest maize area (ha)	450,766.60	424,715.59	329,557.85	432,422.91

The classification of the second-harvest corn areas with Planet images deviated from the results of the other sensors, with a total area for this class of 330,000 hectares, indicating that despite the higher spatial resolution, the classification algorithm confused the second-harvest corn crop with the other second-harvest crop (Table 2). Considering the analysis of variance and Tukey test’s for means comparison, there was no significant difference at 5% probability among the results of the classifications performed, implying that the responses of the sensors were statistically similar (Table 3).

Table 3. Analysis of variance (ANOVA) and means multiple comparison by Tukey's test at 5% probability for the overall accuracy and kappa coefficient results.

Analysis of Variance						
Variable	N	Mean	SD	SE	95% Conf	Interval
MODIS	2	84.42	3.42	2.42	53.72	115.12
Landsat-8	2	86.63	2.86	2.02	60.95	112.31
Planet	2	84.43	3.35	2.37	54.37	114.49
Sentinel-2	2	83.84	3.64	2.57	51.18	116.50
Tukey's test HSD						
Group 1	Group2	Meandiff	P-adj	Lower	Upper	Interval
Landsat-8	MODIS	-2.2098	0.9	-15.7536	11.3339	False
Landsat-8	Planet	-2.2037	0.9	-15.7474	11.34	False
Landsat-8	Sentinel-2	-2.7929	0.8225	-16.3367	10.7508	False
MODIS	Planet	0.0061	0.9	-13.5376	13.5498	False
MODIS	Sentinel-2	-0.5831	0.9	-14.1268	12.9606	False
Planet	Sentinel-2	-0.5892	0.9	-14.1329	12.9545	False

Despite the lower spatial resolution in relation to the other sensors, MODIS images showed values very close to those of the OLI/Landsat sensor, obtaining OA and kappa coefficients of 86.83% and 82.01% (Table 2), respectively, with the focus class of the study having CA (consumer accuracy) of 90.85% and PA (producer accuracy) of 89.40%.

The independence of spatial resolution with LULC classification accuracy were seen in the comparison between the OA and kappa coefficient results of MODIS and MSI/Sentinel-2 sensors, indicating that high-spatial-resolution data are not always superior to low-resolution data in identifying land uses when objects have varied and complex attributes [25,33,52].

The PlanetScope imagery, despite its high spatial resolution, reached inferior overall results compared to OLI/Landsat-8 [33]. This result is probably related to the lower temporal and spectral resolution of this dataset and to the training points being collected in a concentrated manner and not spread over the entire area of interest [56]. This combination of factors did not produce enough information to adequately differentiate the classes, suggesting that the spatial resolution of 4.77 m did not provide enough textural information for the effective separation of the classes studied. The results of Planet NICFI images in relation to Sentinel-2 were similar to each other in both the OA of 86.79% and 86.41%, and kappa of 82.06% and 81.26%, respectively. For CA, the results were higher than 87% and for PA higher than 89%.

Classification in a highly heterogeneous and fragmented agricultural region is challenging due to the similarities in reflectance among the second-crop crops as well as the different temporal and spatial resolutions of the images used. Given this situation, the combination of several types of images with spatial and temporal resolution as well as the use of time series images can be seen in past research, in which better results were achieved than those obtained by analyses using separate, once-monthly images [55,57,58].

Based on our studies, the result obtained in this research, especially for Landsat 8 and MODIS Terra images, is very consistent with respect to classification accuracy and suggests the use in further studies of the combination of the aforementioned images with PlanetScope NIFCI and Sentinel-2 images as well as other sensors in order to achieve more refined results than the present study.

The results of this study were obtained due to the open-access remote sensing datasets and the computing power of the GEE platform, which has demonstrated considerable versatility and adaptability due to its integrative capabilities and its efficient platform for scripting in JavaScript and Python. This study was based on the use of open-source technologies with a focus on processes, and these are robust and scalable over large spatial extents; thus, good results were obtained.

4. Conclusions

The evaluations performed showed satisfactory results since the kappa coefficient and OA presented values higher than 80%. Therefore, it is concluded that the GEOBIA methodology, which employed the combination SNIC + GLCM with the random forest classifier, was successful. However, it is important to highlight that there is still room for improvement in the segmentation step in order to make the methodology applicable in large agricultural areas. The use of other techniques with more spectral models as well as using other types of sensors in the geo-object-oriented analysis input could improve our findings. For future work, the use of hyperspectral data to improve identification should be considered.

Furthermore, this study highlighted the overall reliability of the GEOBIA methodology, although its complexity results in higher computational demands. This can affect the execution of the GEE code, especially when using high-spatial-resolution data such as that from Sentinel-2 and PlanetScope.

Author Contributions: Conceptualization, C.A.d.S.J. and I.C.M.J.; methodology, C.A.d.S.J. and I.C.M.J.; software, R.D., C.L.B. and P.E.T.; validation, C.A.d.S.J., I.C.M.J. and L.P.R.T.; formal analysis, F.S.R. and C.A.d.S.J.; investigation, I.C.M.J.; resources, C.A.d.S.J., J.F.d.O.-J. and M.L.; data curation, J.L.D.-S. and F.H.R.B.; writing—original draft preparation, I.C.M.J. and C.A.d.S.J.; writing—review and editing, P.E.T., L.P.R.T., F.S.R. and J.L.D.-S.; visualization, R.D. and J.F.d.O.-J.; supervision, C.A.d.S.J. All authors have read and agreed to the published version of the manuscript.

Funding: This research received no external funding.

Data Availability Statement: The datasets generated during and/or analyzed during the current study are available from the corresponding author on reasonable request.

Acknowledgments: This study was financed in part by the Coordenação de Aperfeiçoamento de Pessoal de Nível Superior—Brasil (CAPES)—Finance Code 001, National Council for Research and Development (CNPq). We would also like to thank the anonymous reviewers for providing insights to improve the manuscript. We are also thankful to the research laboratory of the State University of Mato Grosso (UNEMAT)—<https://pesquisa.unemat.br/gaaf/> (accessed on 12 December 2022). Thanks to Fundação de Apoio ao Desenvolvimento do Ensino, Ciência e Tecnologia do Estado de Mato Grosso (FAPEMAT) for the financial support of the research project (0001464/2022 and 000125/2023) and Fundação de Apoio ao Desenvolvimento do Ensino and Ciência e Tecnologia do Estado de Mato Grosso do Sul (FUNDECT), numbers 88/2021 and 07/2022, and SIAFEM numbers 30478 and 31333; and CNPq Research Productivity Scholars (processes 309250/2021-8; 306022/2021-4; 303767/2020-0; 304979/2022-8).

Conflicts of Interest: The authors declare that they have no known competing financial interests or personal relationships that could have appeared to influence the work reported in this paper.

References

1. Conab-Boletim Da Safra de Grãos. Available online: <https://www.conab.gov.br/info-agro/safras/graos/boletim-da-safra-de-graos> (accessed on 30 October 2022).
2. Comexstat Exportação e Importação Geral. Available online: <http://comexstat.mdic.gov.br/pt/geral/37761> (accessed on 5 July 2021).
3. CONAB Acompanhamento Da Safra Brasileira. *Cia. Nac. Abast. Acompan. Safra Bras.* **2022**, *7*, 1–89.
4. Bertolin, N.d.O.; Filgueiras, R.; Venancio, L.P.; Mantovani, E.C. Predição da produtividade de milho irrigado com auxílio de imagens de satélite. *Rev. Bras. Agric. Irrig.* **2017**, *11*, 1627–1638. [CrossRef]
5. Oldoni, L.V. *Mapeamento de Soja e Milho Com Mineração de Dados e Imagens Sintéticas Landsat e MODIS. Dissertação*; Universidade Estadual do Oeste do Paraná—Campus de Cascavel: Cascavel, Brazil, 2018.
6. Pino, F.A. *IEA-Instituto de Economia Agrícola-Informações Econômicas*; IEA: São Paulo, Brazil, 2001; Volume 31, pp. 55–58.
7. Oldoni, L.V.; Sanches, I.D.; Picoli, M.C.A.; Covre, R.M.; Fronza, J.G. LEM+ Dataset: For Agricultural Remote Sensing Applications. *Data Brief* **2020**, *33*, 106553. [CrossRef]

8. Prudente, V.H.R.; Martins, V.S.; Vieira, D.C.; Silva, N.R.d.F.; Adami, M.; Sanches, I.D.A. Limitations of Cloud Cover for Optical Remote Sensing of Agricultural Areas across South America. *Remote Sens. Appl.* **2020**, *20*, 100414. [CrossRef]
9. Khadim, F.K.; Su, H.; Xu, L.; Tian, J. Soil Salinity Mapping in Everglades National Park Using Remote Sensing Techniques and Vegetation Salt Tolerance. *Phys. Chem. Earth* **2019**, *110*, 31–50. [CrossRef]
10. Speranza, E.A.; Grego, C.R.; Gebler, L. Analysis of Pest Incidence on Apple Trees Validated by Unsupervised Machine Learning Algorithms. *Rev. Eng. Na Agric. Reveng* **2022**, *30*, 63–74. [CrossRef]
11. de Oliveira, G.; Chen, J.M.; Mataveli, G.A.V.; Chaves, M.E.D.; Seixas, H.T.; da Cardozo, F.S.; Shimabukuro, Y.E.; He, L.; Stark, S.C.; dos Santos, C.A.C. Rapid Recent Deforestation Incursion in a Vulnerable Indigenous Land in the Brazilian Amazon and Fire-Driven Emissions of Fine Particulate Aerosol Pollutants. *Forests* **2020**, *11*, 829. [CrossRef]
12. Mollick, T.; Azam, M.G.; Karim, S. Geospatial-Based Machine Learning Techniques for Land Use and Land Cover Mapping Using a High-Resolution Unmanned Aerial Vehicle Image. *Remote Sens. Appl.* **2023**, *29*, 100859. [CrossRef]
13. Liu, B.; Song, W. Mapping Abandoned Cropland Using Within-Year Sentinel-2 Time Series. *Catena* **2023**, *223*, 106924. [CrossRef]
14. Immitzer, M.; Atzberger, C.; Koukal, T. Tree Species Classification with Random Forest Using Very High Spatial Resolution 8-Band WorldView-2 Satellite Data. *Remote Sens.* **2012**, *4*, 2661–2693. [CrossRef]
15. Gorelick, N.; Hancher, M.; Dixon, M.; Ilyushchenko, S.; Thau, D.; Moore, R. Google Earth Engine: Planetary-Scale Geospatial Analysis for Everyone. *Remote Sens. Environ.* **2017**, *202*, 18–27. [CrossRef]
16. Google Earth Engine Google Earth Engine Platform. Available online: <https://earthengine.google.com/platform/> (accessed on 21 January 2023).
17. SIDRA Levantamento Sistemático Da Produção Agrícola-Setembro. 2020. Available online: <https://sidra.ibge.gov.br/home/lspa/mato-grosso> (accessed on 25 June 2021).
18. IBGE Cidades e Estados-Instituto Brasileiro de Geografia e Estatística. Available online: <https://cidades.ibge.gov.br/brasil/mt/canarana/panorama> (accessed on 24 June 2021).
19. Alves, H.Q.; Rezende, A.C.P.; Sposito, R.d.C. Geoprocessamento Como Ferramenta de Conservação de Recursos Hídricos e de Biodiversidade: Um Estudo de Caso Para o Município de Canarana—MT. *An. XIV Simpósio Bras. Sensoriamento Remoto INPE* **2009**, *14*, 3439–3446.
20. Funk, C.; Peterson, P.; Landsfeld, M.; Pedreros, D.; Verdin, J.; Shukla, S.; Husak, G.; Rowland, J.; Harrison, L.; Hoell, A.; et al. The Climate Hazards Infrared Precipitation with Stations—A New Environmental Record for Monitoring Extremes. *Sci. Data* **2015**, *2*, 150066. [CrossRef] [PubMed]
21. Embrapa. *Embrapa Solos Sistema Brasileiro de Classificação de Solos*, 3rd ed.; Santos, H.G.d., Jacomine, P.K.T., Anjos, L.H.C.d., Oliveira, V.Á.d., Lumbrreras, J.F., Coelho, M.R., Almeida, J.A.d., Cunha, T.J.F., Oliveira, J.B.d., Eds.; Embrapa: Brasília, Brazil, 2013; ISBN 9788570351982.
22. Ferreira, J.C.V.; de Moura e Silva, J.; Silva, P.P.C.; Alencastro, A. *Mato Grosso e Seus Municípios*; Editora Buriti: Buriticupú, Brazil, 2001.
23. MapBiomas Mapas de Referência. Available online: <https://mapbiomas.org/mapas-de-referencia> (accessed on 10 July 2021).
24. Richter, R.; Kellenberger, T.; Kaufmann, H. Comparison of Topographic Correction Methods. *Remote Sens.* **2009**, *1*, 184–196. [CrossRef]
25. Tassi, A.; Gigante, D.; Modica, G.; di Martino, L.; Vizzari, M. Pixel- vs. Object-Based Landsat 8 Data Classification in Google Earth Engine Using Random Forest: The Case Study of Maiella National Park. *Remote Sens.* **2021**, *13*, 2299. [CrossRef]
26. Belcore, E.; Piras, M.; Wozniak, E. Specific alpine environment land cover classification methodology: Google earth engine processing for sentinel-2 data. *Int. Arch. Photogramm. Remote Sens. Spat. Inf. Sci.* **2020**, *XLIII-B3-2*, 663–670. [CrossRef]
27. Shepherd, J.D.; Dymond, J.R. Correcting Satellite Imagery for the Variance of Reflectance and Illumination with Topography. *Int. J. Remote Sens.* **2003**, *24*, 3503–3514. [CrossRef]
28. Ngula Niipele, J.; Chen, J. The Usefulness of Alos-Palsar Dem Data for Drainage Extraction in Semi-Arid Environments in The Iishana Sub-Basin. *J. Hydrol. Reg. Stud.* **2019**, *21*, 57–67. [CrossRef]
29. Farr, T.G.; Rosen, P.A.; Caro, E.; Crippen, R.; Duren, R.; Hensley, S.; Kobrick, M.; Paller, M.; Rodriguez, E.; Roth, L.; et al. The Shuttle Radar Topography Mission. *Rev. Geophys.* **2007**, *45*, 1–33. [CrossRef]
30. Silva, C.A.; Nanni, M.R.; Teodoro, P.E.; Silva, G.F.C. Vegetation Indices for Discrimination of Soybean Areas: A New Approach. *Agron. J.* **2017**, *109*, 1331–1343. [CrossRef]
31. Silva Junior, C.A.d.; Nanni, M.R.; Oliveira-Júnior, J.F.d.; Cezar, E.; Teodoro, P.E.; Delgado, R.C.; Shiratsuchi, L.S.; Shakir, M.; Chicati, M.L. Object-Based Image Analysis Supported by Data Mining to Discriminate Large Areas of Soybean. *Int. J. Digit Earth* **2019**, *12*, 270–292. [CrossRef]
32. Rege, A.; Warnekar, S.B.; Lee, J.S.H. Mapping Cashew Monocultures in the Western Ghats Using Optical and Radar Imagery in Google Earth Engine. *Remote Sens. Appl.* **2022**, *28*, 100861. [CrossRef]
33. Tassi, A.; Vizzari, M. Object-Oriented LULC Classification in Google Earth Engine Combining SNIC, GLCM, and Machine Learning Algorithms. *Remote Sens.* **2020**, *12*, 3776. [CrossRef]

34. Silva Junior, C.A. *Estimativa e Discriminação de Áreas de Soja [Glycine max L.] No Estado Do Paraná Com Dados Mono e Multitemporais do Sensor MODIS. Dissertação*; Universidade Estadual de Maringá: Maringá, Brazil, 2014.
35. Estornell, J.; Martí-Gavliá, J.M.; Sebastiá, M.T.; Mengual, J. Principal Component Analysis Applied to Remote Sensing. *Model. Sci. Educ. Learn.* **2013**, *6*, 83. [[CrossRef](#)]
36. Jia, X.; Richards, J.A. Segmented Principal Components Transformation for Efficient Hyperspectral Remote-Sensing Image Display and Classification. *IEEE Trans. Geosci. Remote Sens.* **1999**, *37*, 538–542. [[CrossRef](#)]
37. Meneses, P.R.; Almeida, T. *Introdução ao Processamento de Imagens de Sensoriamento Remoto*. UnB-CNPq. Brasília. 2012. Available online: https://edisciplinas.usp.br/pluginfile.php/5550408/mod_resource/content/3/Livro-SensoriamentoRemoto.pdf (accessed on 30 October 2022).
38. Achanta, R.; Susstrunk, S. Superpixels and Polygons Using Simple Non-Iterative Clustering. In Proceedings of the 2017 IEEE Conference on Computer Vision and Pattern Recognition (CVPR), Honolulu, HI, USA, 21–26 July 2017; IEEE: Piscataway, NJ, USA; pp. 4895–4904.
39. Amani, M.; Kakooei, M.; Moghimi, A.; Ghorbanian, A.; Ranjgar, B.; Mahdavi, S.; Davidson, A.; Fiset, T.; Rollin, P.; Brisco, B.; et al. Application of Google Earth Engine Cloud Computing Platform, Sentinel Imagery, and Neural Networks for Crop Mapping in Canada. *Remote Sens.* **2020**, *12*, 3561. [[CrossRef](#)]
40. Luo, C.; Qi, B.; Liu, H.; Guo, D.; Lu, L.; Fu, Q.; Shao, Y. Using Time Series Sentinel-1 Images for Object-Oriented Crop Classification in Google Earth Engine. *Remote Sens.* **2021**, *13*, 561. [[CrossRef](#)]
41. Cheng, X.; Liu, W.; Zhou, J.; Wang, Z.; Zhang, S.; Liao, S. Extraction of Mountain Grasslands in Yunnan, China, from Sentinel-2 Data during the Optimal Phenological Period Using Feature Optimization. *Agronomy* **2022**, *12*, 1948. [[CrossRef](#)]
42. Chaves, M.E.D.; Picoli, M.C.A.; Sanches, I.D. Recent Applications of Landsat 8/OLI and Sentinel-2/MSI for Land Use and Land Cover Mapping: A Systematic Review. *Remote Sens.* **2020**, *12*, 3062. [[CrossRef](#)]
43. Wessels, K.J.; Bergh, F.V.D.; Roy, D.P.; Salmon, B.P.; Steenkamp, K.C.; MacAlister, B.; Swanepoel, D.; Jewitt, D. Rapid Land Cover Map Updates Using Change Detection and Robust Random Forest Classifiers. *Remote Sens.* **2016**, *8*, 888. [[CrossRef](#)]
44. Castillejo-González, I.L.; López-Granados, F.; García-Ferrer, A.; Peña-Barragán, J.M.; Jurado-Expósito, M.; de la Orden, M.S.; González-Audicana, M. Object- and Pixel-Based Analysis for Mapping Crops and Their Agro-Environmental Associated Measures Using QuickBird Imagery. *Comput. Electron. Agric.* **2009**, *68*, 207–215. [[CrossRef](#)]
45. Xu, R. Mapping Rural Settlements from Landsat and Sentinel Time Series by Integrating Pixel-and Object-Based Methods. *Land* **2021**, *10*, 244. [[CrossRef](#)]
46. da Silva Junior, C.A.; Moreira, E.P.; Frank, T.; Moreira, M.A.; Barcellos, D. Comparação de Áreas de Soja (*Glycinemax* (L.) Merr.) Obtidas Por Meio Da Interpretação de Imagens TM/Landsat e MODIS/Terra No Município de Maracaju (MS) = Comparison of Areas of Soybean (*Glycine Max* (L) Merr.) Obtained through the Interpretation. *Biosci. J.* **2014**, *30*, 707–716.
47. Silva, C.O. *Da Geoprocessamento Aplicado ao Zoneamento Agrícola Para cana-de-Açúcar Irrigada do Estado do Piauí*; Faculdade de Ciências Agrônomicas da UNESP: Botucatu, Brazil, 2016.
48. Manzatto, C.V.; Assad, E.D.; Bacca, J.F.M.; Zaroni, M.J.; Pereira, N.R. Zoneamento Agroecológico da Cana-de-Açúcar: Expandir a produção, preservar a vida, garantir o futuro. Embrapa Solos. 2009. Available online: <https://ainfo.cnptia.embrapa.br/digital/bitstream/CNPS-2010/14408/1/ZonCana.pdf> (accessed on 30 October 2022).
49. Garcia, Y.M.; Campos, S.; Tagliarini, F.S.N.; Campos, M.; Rodrigues, B.T. Declividade e potencial para mecanização agrícola da bacia hidrográfica do ribeirão pederneiras-pederneiras/sp. *Rev. Bras. Eng. Biosistemas* **2020**, *14*, 62–72. [[CrossRef](#)]
50. Anece, I.; Thenkabail, P. Accuracies Achieved in Classifying Five Leading World Crop Types and Their Growth Stages Using Optimal Earth Observing-1 Hyperion Hyperspectral Narrowbands on Google Earth Engine. *Remote Sens.* **2018**, *10*, 2027. [[CrossRef](#)]
51. Zhang, C.; Li, X.; Wu, M.; Qin, W.; Zhang, J. Object-Oriented Classification of Land Cover Based on Landsat 8 OLI Image Data in the Kunyu Mountain. *Sci. Geogr. Sin.* **2018**, *38*, 1904–1913.
52. Ruiz, L.F.C.; Guasselli, L.A.; Simioni, J.P.D.; Belloli, T.F.; Barros Fernandes, P.C. Object-Based Classification of Vegetation Species in a Subtropical Wetland Using Sentinel-1 and Sentinel-2A Images. *Sci. Remote Sens.* **2021**, *3*, 100017. [[CrossRef](#)]
53. Stromann, O.; Nascetti, A.; Yousif, O.; Ban, Y. Dimensionality Reduction and Feature Selection for Object-Based Land Cover Classification Based on Sentinel-1 and Sentinel-2 Time Series Using Google Earth Engine. *Remote Sens.* **2019**, *12*, 76. [[CrossRef](#)]
54. Maxwell, A.E.; Strager, M.P.; Warner, T.A.; Ramezan, C.A.; Morgan, A.N.; Pauley, C.E. Large-Area, High Spatial Resolution Land Cover Mapping Using Random Forests, GEOBIA, and NAIP Orthophotography: Findings and Recommendations. *Remote Sens.* **2019**, *11*, 1409. [[CrossRef](#)]
55. El Imanni, H.S.; El Harti, A.; Hssaisoune, M.; Velastegui-Montoya, A.; Elbouzidi, A.; Addi, M.; El Iysaouy, L.; El Hachimi, J. Rapid and Automated Approach for Early Crop Mapping Using Sentinel-1 and Sentinel-2 on Google Earth Engine; A Case of a Highly Heterogeneous and Fragmented Agricultural Region. *J. Imaging* **2022**, *8*, 316. [[CrossRef](#)]
56. Della-Silva, J.L.; da Silva Junior, C.A.; Lima, M.; Teodoro, P.E.; Nanni, M.R.; Shiratsuchi, L.S.; Teodoro, L.P.R.; Capristo-Silva, G.F.; Baio, F.H.R.; de Oliveira, G.; et al. CO2Flux Model Assessment and Comparison between an Airborne Hyperspectral Sensor and Orbital Multispectral Imagery in Southern Amazonia. *Sustainability* **2022**, *14*, 5458. [[CrossRef](#)]

57. Inglada, J.; Vincent, A.; Arias, M.; Marais-Sicre, C. Improved Early Crop Type Identification By Joint Use of High Temporal Resolution SAR And Optical Image Time Series. *Remote Sens.* **2016**, *8*, 362. [[CrossRef](#)]
58. Luo, C.; Liu, H.; Lu, L.; Liu, Z.; Kong, F.; Zhang, X. Monthly Composites from Sentinel-1 and Sentinel-2 Images for Regional Major Crop Mapping with Google Earth Engine. *J. Integr. Agric.* **2021**, *20*, 1944–1957. [[CrossRef](#)]

Disclaimer/Publisher’s Note: The statements, opinions and data contained in all publications are solely those of the individual author(s) and contributor(s) and not of MDPI and/or the editor(s). MDPI and/or the editor(s) disclaim responsibility for any injury to people or property resulting from any ideas, methods, instructions or products referred to in the content.